

FLYNN: Robust Neural Network for Robot Navigation using Fly Brain Topology

Benquan Wang¹ and Jingdao Chen²

Abstract—While deep learning models achieve state-of-the-art performance in complex tasks, they remain brittle when faced with new environments or sensory deprivation. In contrast, biological systems exhibit remarkable tolerance to these challenges. We address this vulnerability by developing a recurrent neural network (RNN) whose architecture is directly derived from the synaptic-resolution brain connectome of the fruit fly *Drosophila melanogaster*. We demonstrate the feasibility of training the fly connectome neural network (FLYNN) to perform vision-based navigation in MuJoCo, achieving performance comparable to modern hand-crafted networks of similar parameter counts. Crucially, FLYNN exhibits superior resistance to out-of-distribution (OOD) data and tolerance to sensory loss without further training. It remained functional even under total vision loss while hand-crafted networks largely failed, even when specifically trained with camera dropout. Principal Component Analysis (PCA) of the internal state of FLYNN suggests that it exhibits a particularly high degree of representational modularity, which might be related to its robustness. Our work provides a new direction for designing resilient artificial agents following the topology of biological brains.

I. INTRODUCTION

Artificial Neural Networks (ANNs) originated from biologically inspired artificial neurons [1]. Since their inception, researchers have engineered increasingly sophisticated architectures to address complex challenges such as voice recognition, image classification, and navigation. Although the detailed structures of modern ANNs are primarily hand-crafted, the biological brain remains a foundational source of inspiration. The Convolutional Neural Network (CNN) [2], [3] is a prominent example of this influence, followed by other notable architectures including Recurrent Neural Networks (RNNs) [4], Long Short-Term Memory (LSTM) units [5], and Transformers [6]. Following decades of development, state-of-the-art ANN architectures now frequently outperform humans on a wide range of complex tasks.

Navigation is one of the areas in which robustness is critical. While current state-of-the-art ANN models perform well under ideal conditions, they are known to be vulnerable to out-of-distribution (OOD) data [7] and sensor information degradation or deprivation. In modern autonomous driving systems, for example, encountering a never-seen-before situation or suffering the loss of a camera stream typically triggers an immediate emergency handover, as the underlying

models are designed to rely on the continuous integration of all available inputs [8] according to their trained policies.

In contrast, biological organisms exhibit extraordinary robustness to all of these failure modes. For example, animals are known to adapt to new environments without difficulty. An animal that loses an eye can typically adapt quickly and maintain its ability to navigate the environment. Such resilience is likely rooted in the distinctive architecture of the biological brain. In *Drosophila*, for instance, the visual system is composed of distinct, highly organized neuropils – including the lamina, medulla, lobula plate, and lobula – specialized for calculating optical flow from visual input [9], [10]. Furthermore, the central complex of the *Drosophila* brain contains a population of ring neurons that serve as a heading direction calculator for navigation [11], [12]. These well-organized structures serve as a structural prior that enables the organism to maintain stable internal representations of space even in unknown environments or under sensory deprivation.

Extensive studies have focused on improving OOD generalization of ANN models for robust navigation. Efforts include designing specialized training strategies like domain randomization [13], [14], and developing new network architectures like liquid neural networks [15], [16]. Large language models have also been explored for robust navigation tasks [17], [18]. Many studies have also focused on enhancing model tolerance to image degradation, occlusion, and total sensor loss [19], [20], [21]. However, maintaining navigational robustness in new environments or during camera failure remains significant challenges. The extraordinary resilience exhibited by biological organisms, combined with the recent availability of the complete *Drosophila* (fruit fly) connectome [22], [23] – the first and only connectome of an animal with a complex vision system – presents a unique opportunity to develop a biologically faithful architecture specifically designed to address these challenges. To our knowledge, this is the first study to exploit the *Drosophila* connectome in the context of robot navigation tasks. Most existing works have focused on using biologically realistic simulations to investigate and understand the mechanisms of different systems of the brain, for example, the visual system [24] and the taste system [25], [26].

In this work, we translated the synaptic-resolution *Drosophila* connectome into an RNN. By constraining the network’s connectivity to this biological blueprint, we inherited the functional redundancy and modularity characteristic of biological systems. We evaluated the fly connectome neural network (FLYNN) in a simulated MuJoCo environ-

¹Benquan Wang is with the Department of Computer Science Engineering, Mississippi State University, Mississippi State, MS 39762, USA bw1918@msstate.edu

²Jingdao Chen is with the Department of Computer Science Engineering, Mississippi State University, Mississippi State, MS 39762, USA chenjingdao@cse.msstate.edu

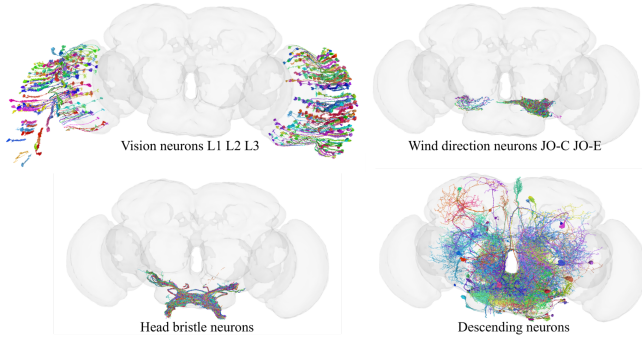


Fig. 1. Subsets of sensory neurons and descending neurons used in this work in the FAFB v783 connectome dataset. Credit: FlyWire.ai.

ment [27], compared it against standard networks of similar parameter sizes such as EfficientNet-B0 [28], MobileNet-large-v3 [29], and small-world RNN [30], and investigated the sources of robustness in biological neural architectures.

Our results demonstrate three key findings:

- 1) Feasibility: An RNN architecture constrained strictly by biological connectivity can be trained to perform complex tasks, such as vision-based multi-sensory navigation.
- 2) Competitive Performance: The FLYNN achieved performance levels comparable to modern hand-crafted models of similar parameter counts.
- 3) Graceful Degradation: Most notably, same as biological organisms, the FLYNN exhibits unique robustness to out-of-distribution (OOD) data and sensor ablation even though it was never trained for this.

II. METHODS

At the core of FLYNN is the RNN constructed from all the connections in the connectome. Sensory inputs were passed into corresponding sensory neurons in the RNN, and motion commands were extracted from descending neurons via a multilayer perceptron (MLP) that generated robot control outputs. All the sensory neurons and descending neurons used in this work as seen in the *Drosophila* brain of the connectome dataset are illustrated in Fig. 1. The overall structure of the FLYNN is shown in Fig. 2.

A. From Connectome to RNN

The *Drosophila* connectome dataset was released in 2024 [22], [23] and is publicly accessible via the FlyWire.ai platform. This is a seminal result in biology in which the neuronal wiring diagram of the complete brain of a multicellular organism was precisely mapped by acquiring and analyzing brain images obtained via electron microscopy. Our work utilizes the “FAFB v783” version of the connectome, derived from a female adult *Drosophila*, and contained all the connections with no less than five synapses. The entire connectome comprised 139,255 neurons and 5,342,445 connections, and was structured as an edge list, where each entry specifies the pre-synaptic neuron ID, post-synaptic neuron ID, and the corresponding synapse count.

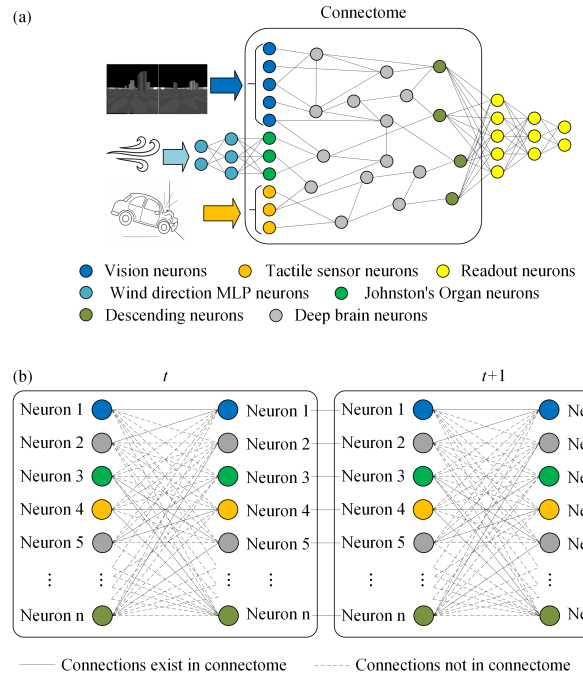


Fig. 2. Structure of the FLYNN. (a) Diagram showing the connectome network and its inputs and outputs. (b) Diagram showing the RNN built from the connectome. Sensor input, bias, and activation function were not included for simplicity.

We employed a simple leaky integrator neuron model to construct the network. Specifically, the hidden state h of the neurons at time $t + 1$ is defined by the following recurrence relation:

$$h^{t+1} = \alpha \odot h^t + (1 - \alpha) \odot \tanh(W h^t + x^t + b) \quad (1)$$

$$W = \begin{bmatrix} w_{1,1} & w_{1,2} & w_{1,3} & \cdots & w_{1,n} \\ w_{2,1} & w_{2,2} & w_{2,3} & \cdots & w_{2,n} \\ w_{3,1} & w_{3,2} & w_{3,3} & \cdots & w_{3,n} \\ \vdots & \vdots & \vdots & \ddots & \vdots \\ w_{n,1} & w_{n,2} & w_{n,3} & \cdots & w_{n,n} \end{bmatrix}$$

$$h^t = \begin{bmatrix} h_1^t \\ h_2^t \\ h_3^t \\ \vdots \\ h_n^t \end{bmatrix}, \quad x^t = \begin{bmatrix} x_1^t \\ x_2^t \\ x_3^t \\ \vdots \\ x_n^t \end{bmatrix}, \quad b = \begin{bmatrix} b_1 \\ b_2 \\ b_3 \\ \vdots \\ b_n \end{bmatrix}$$

$$\alpha = \begin{bmatrix} \alpha_{\text{class.of.neuron.1}} \\ \alpha_{\text{class.of.neuron.2}} \\ \alpha_{\text{class.of.neuron.3}} \\ \vdots \\ \alpha_{\text{class.of.neuron.n}} \end{bmatrix}$$

where \odot denotes element-wise multiplication, W represents the synaptic weight matrix, and h^t denotes the states of all neurons at time t . The vector x^t represents sensory

inputs. Because only a small subset of neurons receives environmental stimuli, most elements of x^t are zero. Finally, b and α represent the biases and leak rates of the neurons, respectively, with the constraint that neurons of the same class share a uniform leak rate. The class of each neuron is available in the connectome dataset.

At its core, the FLYNN is a biologically-constrained recurrent architecture representing the full FAFB v783 *Drosophila* connectome. Unlike conventional multilayered networks, this network utilizes a single hidden state vector h^t that evolves according to a synaptic connectivity matrix W directly derived from the connectome. Since most possible neural connections in W do not exist in the connectome, the matrix W is characterized by extreme topological sparsity (99.9725%), where nonzero weights are assigned only to verified biological connections, as illustrated in Fig. 2(b). In this configuration, network depth is an emergent property of temporal propagation and integration: as discrete time-steps progress, signals propagate from sensory neurons through intermediate deep brain circuits to descending motor neurons. By representing the entire connectome as a sparse matrix, we preserved all complex, nonhierarchical connectome structures, such as the ring attractor [11], [12], that are essential for stable heading and navigation.

B. Input and Output

To enable effective navigation, we integrated three essential sensory modalities—vision, wind direction, and tactile information—into the network, allowing the robot to see obstacles, orient toward the target, and detect collisions.

Visual input was provided via images captured from two simulated onboard cameras of the robot. While visual data could theoretically be mapped to the *Drosophila* photoreceptors, incomplete connectivity data for approximately half of the photoreceptors in the left eye rendered this approach infeasible. Instead, we bypassed the photoreceptor layer and mapped visual inputs directly to photoreceptors’ primary downstream targets: the L1, L2, and L3 neurons [9]. Camera images were first spatially sampled according to the anatomical positions of these L neurons, and the resulting intensity values were then transmitted to respective L neurons. The anatomical positions of L neurons are available in the connectome dataset. Because L1 and L2 neurons primarily detect motion edges, their inputs underwent temporal filtering to enhance edge contrast before being integrated into their hidden states. Conversely, L3 neurons, which process slow fluctuations in environmental luminance, received inputs that were averaged over time prior to integration.

Drosophila utilizes wind direction as a critical cue to locate food. They move against the wind upon detecting food odors, a behavior known as anemotaxis [31]. Thus, we used wind direction to represent the relative angle from the robot to the target. Wind direction is primarily sensed through the Johnston’s Organ (JO) located in the antennae [32]. While target angle information should ideally be routed directly to JO neurons, the architectural complexity of JO neurons necessitated an intermediate step. Target angle was

first processed by a small MLP, the output of which was then mapped to the JO neurons within the connectome.

In addition to wind sensing, *Drosophila* uses bristle neurons to collect tactile information for collision detection and recovery. Collision data were mapped to specific bristle neurons in the connectome. While bristles are distributed across the entire body, we simplified the input by targeting only those located on the anterior portion of the head. Specifically, a collision on the left side of the head activated all corresponding left-side head bristle neurons. The same logic applied to collisions occurring on the right side of the head.

The descending neurons of *Drosophila* convey motor commands. A small MLP was connected to all descending neurons in the connectome to convert the encoded hidden states into final wheel commands for the robot. 2

C. MuJoCo Environment

We used FLYNN to control a simulated differential drive robot within the environment simulated by the MuJoCo physics engine [27]. The simulation environment used for training the networks and evaluating their robustness to vision loss is depicted in Fig. 3(a1). The walls enclosed a 14×14 m arena populated by 20 randomly distributed cylindrical obstacles. These obstacles had a uniform radius of 0.4 m and were assigned randomized colors. The obstacles, walls, and the floor were textured with checkerboard patterns. The robot was equipped with two grayscale cameras (i.e., eyes), each featuring a 120° field of view (FOV) with a 10° overlap between the two camera FOVs. Representative images as captured by these cameras are illustrated in Fig. 3(a2). Images from the cameras were processed and mapped to the network’s left- and right-side L neurons. The agent’s objective was to locate the “food” target, represented by a white sphere randomly placed within the arena. The target’s relative angle to the robot was computed by the simulation and supplied to FLYNN, while tactile feedback was provided whenever a collision occurred.

We also modified the environment to evaluate the OOD generalization of different models by replacing the checkerboard textures with photo-realistic textures. 3D rendering and camera images of the modified environment are shown in Figs. 3(b1) and (b2). The floor was textured with an image of grassland, the sky was textured with an image of a clear sky, and the obstacles and walls were textured with an image of a concrete surface. This modified environment was used only for OOD generalization evaluation and no model ever saw this environment during training.

D. Model Training

In this study, we used DAgger (Dataset Aggregation) imitation learning [33] to train the FLYNN model to solve navigation tasks in our simulated environment. Imitation learning was used to replicate the process by which organisms learn from past successful experiences, whether through self-exploration or observation of other organisms. All model parameters were trainable, including all the weights and

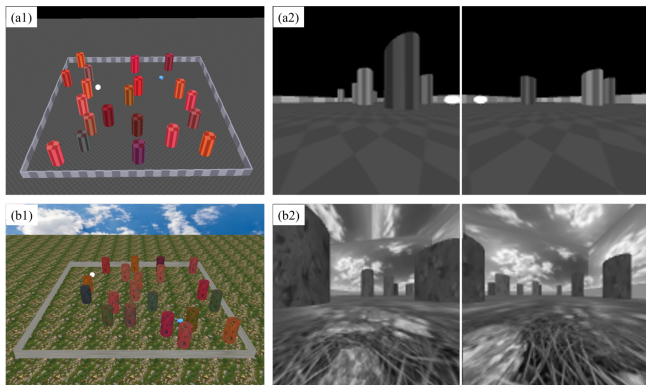


Fig. 3. The simulated MuJoCo environments. The cylinders are obstacles, the white ball is the target, and the short blue cylinder is the robot. (a1) 3D rendering of the environment with checkerboard textures in which the networks were trained and evaluated for vision loss robustness. (a2) The checkerboard textured environment as seen by the left and right cameras on the robot. Camera resolution was set to 128×128 pixels. (b1) 3D rendering of the environment in which the networks were evaluated for out-of-distribution generalization. Realistic textures were applied to obstacles, walls, floor, and sky. Note that no model was trained in this environment. (b2) The realistic textured environment as seen by the left and right cameras on the robot.

biases of FLYNN and the leak rates of every neuron in the connectome. The expert teacher had access to privileged environmental information, including obstacle coordinates, the target location, and the robot’s current pose, while the student only had access to sensory inputs comprising vision, wind direction, and collision signals. The teacher used privileged information to generate optimal paths. These paths were planned using the Vector Field Histogram Star (VFH*) algorithm [34]. As a locally deterministic algorithm, VFH* closely approximates the localized navigational behavior observed in *Drosophila*, in which the organism steers toward a target in smooth trajectories while maintaining a safe distance from locally visible obstacles. The inherent stability and predictability of VFH* ensured high-quality, consistent training data, which was critical for robust model convergence. A Proportional-Integral-Derivative (PID) controller was then employed to translate these paths into target linear velocities and turning rates, which were subsequently converted into individual wheel speeds to drive the robot’s differential wheels.

Training data generated by the teacher were segmented into five behavioral categories: start, pre-collision, collision, straight, and turn. This categorization allowed for controlled sampling, ensuring balanced training datasets. The model underwent four training iterations. At the beginning of each training iteration, 500 new episodes were collected, processed, and added to the cumulative training pool. To ensure generalization, obstacle positions and colors, target location, and initial robot pose were randomized for every episode. In the initial training iteration, the robot was controlled exclusively by the expert teacher, corresponding to a teacher-student mixing ratio of 1.0. To enhance data diversity, random noise (mean level $0.5 \times$ max wheel speed) was injected into the teacher’s control commands for 50 consecutive steps

every 60 steps. Starting with the second iteration, the teacher-student mixing ratio was decreased by 0.5 per iteration, and the injected noise level was reduced by 0.2 per iteration. Each iteration consisted of 300 training steps, with each step comprising 128 batches of data. We employed the Adam optimizer to minimize the Mean Squared Error (MSE) between the teacher’s expert commands and the student’s outputs.

E. Reference Networks

1) *EfficientNet and MobileNet*: We used EfficientNet-B0 [28] and MobileNet-v3-large [29] as baseline models for performance comparison. For brevity, these networks are hereafter referred to as EfficientNet and MobileNet, respectively. These networks were chosen because they have roughly the same parameter counts as FLYNN (~ 5 million), and are known to have a strong balance between speed, latency, and accuracy at low parameter counts.

Both networks were trained on the same navigation task as the FLYNN using the same DAGger framework. Camera images were down-sampled to 30×30 pixels, matching the approximate resolution of the *Drosophila* eye [9]. Images from left and right cameras were then concatenated horizontally before being passed to the models. The original classifiers in these networks were replaced with Gated Recurrent Units (GRUs) followed by an MLP to generate robot control commands. Relative target angle and collision data were integrated as inputs to the GRU as well.

Both EfficientNet and MobileNet were trained with camera dropout since CNNs are known to be sensitive to degraded or lost image input without special treatment. During every training session, in each batch of training data, 20% of chunks had the left side camera turned off, 20% of chunks had the right side camera turned off, and another 20% of chunks had both cameras turned off. This forced the agents to learn to navigate under partial or total vision loss conditions.

2) *Small-World Model*: Animal brains show small-world network topology [35], and it has been shown that random small-world networks could perform complex tasks effectively [36]. Thus, we included a random small-world network as a baseline, referred to as SmallWorldNet, that was designed to closely match important properties of the *Drosophila* connectome.

We utilized the Watts-Strogatz (WS) model [30] to generate a graph with 139,255 nodes and an average degree of 78, matching the total synapse count and sparsity of the connectome dataset. Also, to ensure information propagation geometry was preserved, sensory populations were sampled from communities whose average path length to other sensory communities and descending neurons matched that of the connectome. Comparing FLYNN against this structurally similar yet topologically generic baseline allowed us to isolate the specific contributions of network properties to navigational resilience.

III. RESULTS

The trained FLYNN exhibited *Drosophila*-like navigation behaviors, including target pursuit, obstacle avoidance, and

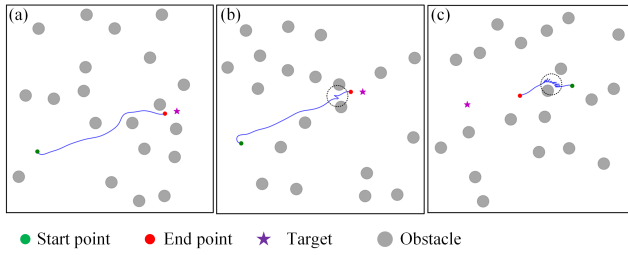


Fig. 4. Representative trajectories of the robot controlled by FLYNN with full vision in the checkerboard textured environment. (a) A successful trajectory without any collisions. (b) A successful trajectory with one collision (dashed circle), and successful recovery from the collision. (c) A failed trajectory with many collisions (dashed circle). The robot eventually recovered from collisions but didn’t have enough time to reach the target.

post-collision recovery (backing up, turning, and moving forward). Representative trajectories of the agent navigating the checkerboard-textured environment toward the target are shown in Fig. 4. Panel (a) shows a representative episode in which the robot successfully navigated around the obstacles and reached the target. In Fig. 4(b) the robot had one collision but was able to recover by backing up, turning, and driving forward, illustrated by the Z-shaped trajectory in the dashed circle. Fig. 4(c) shows a situation in which the robot had repeated collisions, spent too much time recovering from those collisions, and failed to reach the goal within the 600-step limit.

To quantify the performance of the models, each model was used to control the robot for the same set of 300 randomized episodes, in which obstacles were randomly positioned and colored. The robot’s initial position and orientation, as well as the target location, were also randomized. The following parameters were measured for quantifying model performance.

- 1) Success rate: percentage of successful episodes out of the 300 total episodes. An episode was defined as successful if the robot reached the target within 600 steps, regardless of the number of collisions that occurred during the process.
- 2) Success weighted by Path Length (SPL): SPL of episode i is defined as $SPL_i = S_i \frac{L_i^*}{\max(L_i^*, L_i)}$, where L_i^* is the optimal path length calculated by the A* algorithm, and L_i is the actual path length. SPL standard deviation across episodes is not presented here because the SPLs follow a bimodal distribution and standard deviation is not a meaningful measure.
- 3) SPL of successful episodes only.
- 4) Episode duration. One episode would end once the robot reached the target, i.e., the center-to-center distance between the robot and the target was less than 0.8 m. Otherwise the robot would run the entire 600 steps allowed, which corresponds to 12 seconds.
- 5) Collision count per episode.
- 6) Collision count per episode of successful episodes only.

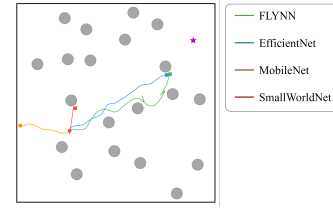


Fig. 5. Example trajectories of models driving the robot in the modified environment with realistic textures.

1) *OOD Generalization*: We tested the OOD generalization capability of all the models by having the models control the robot in the modified environment with realistic textures, which none of the models had ever seen during training, while keeping all sensory input intact. Performance parameters are shown in Table I. While all models performed comparably across all performance metrics in the checkerboard environment, FLYNN demonstrated the best overall performance in the modified environment, showing the best OOD generalization capability. FLYNN had the best numbers on success rate, average SPL, and average episode duration. It had the highest average collision count both overall and within successful episodes. This is consistent with its maintained collision-recovery behavior, which sometimes required multiple attempts, resulting in a higher collision count. The collision count for other models was low because they either partially or entirely lost the collision recovery behavior and would collide with an obstacle and stall. Example trajectories of all models in the modified environment are shown in Fig. 5. FLYNN showed all expected navigation behaviors. EfficientNet did not back up from the collision and stalled. MobileNet and SmallWorldNet both failed entirely, driving in the wrong direction and eventually stalling.

2) *Vision loss tolerance*: We also tested model performance under conditions of partial or total vision loss. This evaluation was conducted in the environment with checkerboard textures, the environment in which the models were trained. Performance parameters of all models are shown in Table II, and also plotted in Fig. 6 for easy comparison. All models achieved similar performance across all measured metrics with intact vision input as shown by the green bars in Fig. 6. (This was the same condition as the checkerboard environment case in the OOD generalization test, so the first four rows of data in Table I and Table II are therefore identical.) Visual inspection of navigation episodes confirmed that all models exhibited the expected navigation behaviors (example trajectories are shown in Fig. 7).

All models showed similar levels of performance degradation when one eye’s vision input was removed as shown by blue and orange bars in Fig. 6. However, note that EfficientNet and MobileNet achieved such robustness through the camera dropout training, whereas FLYNN and SmallWorldNet demonstrated this robustness spontaneously without camera dropout training. We observed that EfficientNet and MobileNet would fail entirely without dropout training, i.e., success rates were 0%.

TABLE I

MODEL PERFORMANCE COMPARISONS UNDER NORMAL (CHECKERBOARD ENVIRONMENT TEXTURE) AND OOD (REALISTIC-IMAGE ENVIRONMENT TEXTURE) VISION DATA (NUMBER OF EPISODES $n = 300$, BEST VALUES IN BOLD.)

Env. Texture	Model	Success %	SPL	SPL Succ.	Episode Dur. (s)	Avg. Coll.	Avg. Coll. Succ.
Checkerboard	FLYNN	92.9	0.83	0.89±0.10	7.2±2.3	0.89±1.64	0.54±0.97
	EfficientNet	90.3	0.80	0.88±0.11	7.6±2.4	1.08±1.57	0.71±1.05
	MobileNet	91.6	0.81	0.89±0.11	7.4±2.4	1.00±1.46	0.67±0.95
	SmallWorldNet	89.0	0.80	0.90±0.10	7.8±2.4	1.12±2.08	0.57±1.11
Realistic image	FLYNN	42.1	0.32	0.75±0.09	10.6±1.9	3.36±1.96	1.53±0.99
	EfficientNet	17.2	0.15	0.90±0.09	11.3±1.8	1.32±1.32	0.38±0.74
	MobileNet	0.0	0.0	N.A.	12.0±0.0	0.65±0.67	N.A.
	SmallWorldNet	3.2	0.02	0.67±0.04	12.0±0.2	1.79±1.48	0.2±0.63

TABLE II

MODEL PERFORMANCE COMPARISONS UNDER DIFFERENT VISION CONDITIONS (NUMBER OF EPISODES $n = 300$, BEST VALUES IN BOLD.)

Vision Condition	Model	Success %	SPL	SPL Succ.	Episode Dur. (s)	Avg. Coll.	Avg. Coll. Succ.
Full vision	FLYNN	92.9	0.83	0.89±0.10	7.2±2.3	0.89±1.64	0.54±0.97
	EfficientNet	90.3	0.80	0.88±0.11	7.6±2.4	1.08±1.57	0.71±1.05
	MobileNet	91.6	0.81	0.89±0.11	7.4±2.4	1.00±1.46	0.67±0.95
	SmallWorldNet	89.0	0.80	0.90±0.10	7.8±2.4	1.12±2.08	0.57±1.11
Left eye only	FLYNN	77.4	0.67	0.87±0.11	8.5±2.7	2.27±2.51	1.21±1.65
	EfficientNet	78.6	0.70	0.89±0.10	8.2±2.7	1.11±1.54	0.64±0.91
	MobileNet	73.5	0.65	0.88±0.10	8.3±2.8	1.11±1.46	0.51±0.76
	SmallWorldNet	46.3	0.40	0.86±0.14	10.2±2.4	0.85±1.17	0.57±0.80
Right eye only	FLYNN	69.6	0.60	0.86±0.12	8.7±2.8	2.46±2.75	0.92±1.42
	EfficientNet	46.6	0.42	0.90±0.10	9.7±2.8	1.77±1.81	0.49±0.84
	MobileNet	58.3	0.53	0.91±0.10	9.0±2.9	1.22±1.85	0.31±0.73
	SmallWorldNet	68.0	0.56	0.82±0.12	9.3±2.4	1.38±1.43	0.66±0.80
Total blindness	FLYNN	44.3	0.37	0.83±0.13	10.3±2.5	4.54±2.88	1.95±1.97
	EfficientNet	3.9	0.03	0.90±0.10	11.8±1.0	1.00±0.27	0.00±0.00
	MobileNet	16.5	0.16	0.96±0.05	11.3±1.8	1.18±0.79	0.88±0.93
	SmallWorldNet	2.6	0.02	0.75±0.08	11.9±0.6	0.72±1.01	1.63±0.74

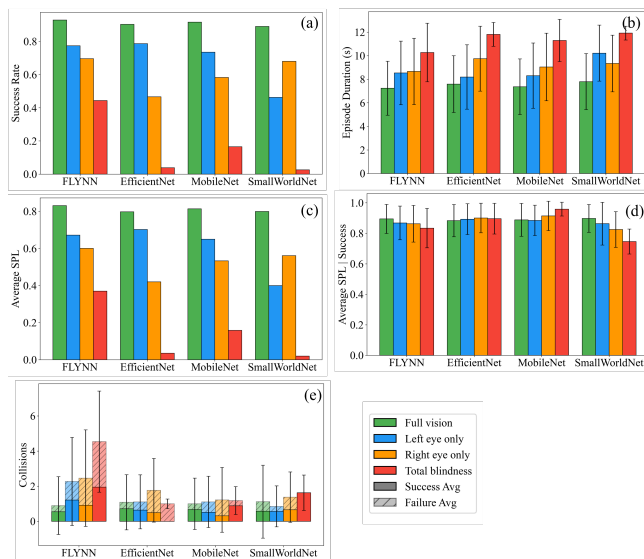


Fig. 6. Performance comparisons of different models under different vision conditions. Number of episodes was 300. (a) Success rate. (b) Average episode duration. (c) Average SPL. (d) Average SPL of successful episodes. (e) Number of collisions per episode. Shadow areas show collision count from failed episodes.

FLYNN showed the highest robustness when vision input from both eyes was lost. As shown by the red bars in Fig. 6(a) and (c), success rate and average SPL collapsed for all networks under total vision loss, except for FLYNN. The high success rate of FLYNN suggests that FLYNN was able to use the remaining sensory inputs, i.e., wind direction and collision information, to maintain its navigational capability. The low episode duration, as shown in Fig. 6(b), suggests that the robot rarely stalled. This agrees with the observed high collision count (Fig. 6(e)). The robot maintained collision recovery behavior, but without the help of vision information, it took more attempts to recover (Fig. 7, red trajectory of FLYNN). In contrast, as shown by the red trajectories in Fig. 7, all models except FLYNN stalled once a collision happened, i.e., collision recovery behavior was lost under total blindness. This agrees with the relatively low collision count as shown in Fig. 6(e).

The high average SPLs of successful episodes across all models and all conditions, as shown in Fig. 6(d), suggests that no model drove the robot along spiral or erratic paths in successful episodes. However, the success rate must be taken into consideration when evaluating SPLs. For example, in the

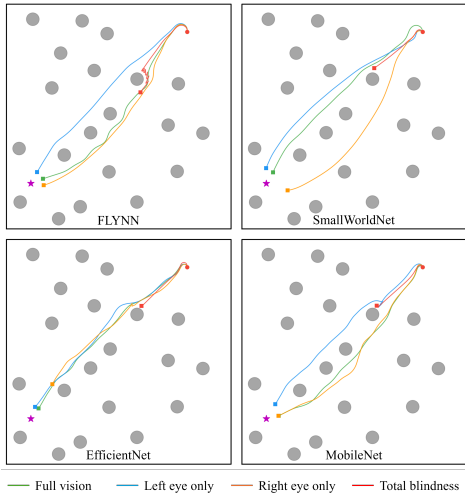


Fig. 7. Example trajectories of models under different vision conditions.

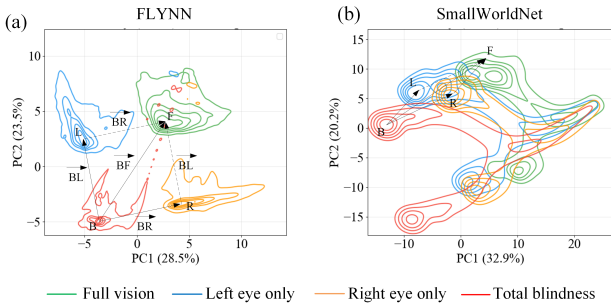


Fig. 8. KDE plots of the first two principal components of (a) FLYNN's and (b) SmallWorldNet's internal states under different vision conditions over 300 episodes.

rare situation where there is no obstacle between the robot and the target, the episode could turn into a successfully completed episode with high SPL due to a direct path. The high average success SPL thus merely indicates that the models were driving mostly straight.

Notice that similar to FLYNN, SmallWorldNet also showed some resistance to partial vision loss without dropout training. However, it failed almost entirely with total vision loss, whereas FLYNN remained functional. Since both networks shared similar properties – the RNN architecture, small-world property, node degree, distances between sensory neurons and descending neurons – looking into how their internal states differ could provide insights into the source of FLYNN's robustness.

We performed Principal Component Analysis (PCA) on the neuron states of both models as they navigated through the same set of 300 test environments. We then performed Kernel Density Estimation (KDE) on the first two principal components of all the PCA trajectories over 300 episodes. The KDE analysis showed where the models' internal states appear most often in the principal component space when navigating through the episodes. The results are plotted in Fig. 8. It was evident that the internal states of FLYNN

formed distinct clusters under different vision conditions, indicating a clear and stable internal representation for each vision condition. In contrast, SmallWorldNet produced broad, overlapping distributions with high representational entropy.

We found that in FLYNN the sum of the vectors \vec{BL} and \vec{BR} – representing the transitions from KDE peak of the totally blind state B to single-eye states L and R – almost exactly equal to the blind (B) to full-vision (F) states vector \vec{BF} , i.e., $\vec{BF} \approx \vec{BL} + \vec{BR}$ (arrows in Fig. 8(a)). We further numerically checked the relationship between the vectors using the first 10 principal components, which together explained 89.1% total variance for FLYNN and 94.6% for SmallWorldNet. For FLYNN, vector magnitudes were $|\vec{BF}| = 11.16$, $|\vec{BL} + \vec{BR}| = 11.11$, and cosine similarity was 0.9998. For SmallWorldNet, $|\vec{BF}| = 22.88$, $|\vec{BL} + \vec{BR}| = 30.01$, and cosine similarity was 0.9439. The linear sum held almost perfectly for FLYNN and did not hold for SmallWorldNet.

This linear superposition of FLYNN internal states indicates that the *Drosophila* connectome preserves the independent information streams of each sensor, allowing the agent to maintain a coherent navigation logic even when the vision input is partially or entirely removed. Such geometric regularity was absent from the small-world network baseline.

IV. CONCLUSIONS

In conclusion, this research represents the first effort to build an RNN with a network structure strictly constrained by the *Drosophila* connectome topology. We demonstrated that such a network not only could be trained for complex tasks, such as vision-based multi-sensory navigation, but also achieve performance comparable to modern hand-crafted networks. More importantly, such a network showed remarkable OOD generalization and tolerance to vision loss even though the network never encountered such situations during training. The network was able to maintain most of its navigation capability under unfamiliar conditions, outperforming modern hand-crafted networks in simulated navigation tasks.

The fact that SmallWorldNet showed some degree of robustness to partial vision loss suggests that the small-world property, which is shared between SmallWorldNet and FLYNN, may contribute to the observed robustness. However, the small-world property could not explain all of the robustness that FLYNN exhibited. Our KDE analysis of the PCA-projected internal states revealed distinct differences in the internal state distribution between the two networks. The tight clustering observed in the KDE plots and linear summation of different states strongly suggest that the *Drosophila* connectome acted as a topological prior for linear sensory integration. This allowed the agent to gracefully degrade in response to sensor loss without disrupting the global navigation manifold, a function that did not exist in random small-world architectures. Such linear sensory fusion likely stems from the modular and redundant design of the *Drosophila* brain, and could be a potential explanation for

the robustness of FLYNN. The detailed mechanism remains to be explored in future work.

We acknowledge that the FLYNN built in this work is constrained solely by connectome topology, and we used several simplifications to make constructing a functional network from the complex connectome feasible. The properties that exist in biological brains but were not included in our model include, but are not limited to, spiking neurons, electrical synapses, gap junctions, axon length differences, neurotransmitter types, etc. All of these differences could affect the model performance. We expect the model to perform better or more similarly to the behavior of real *Drosophila* if any or all of these factors were included in our model.

Overall, we not only successfully demonstrated the feasibility of training and using FLYNN for navigation tasks, but also showed the superior robustness of FLYNN to OOD data and input deprivation. We envision that this work will pave the way for new directions in biologically inspired robotics and provide a blueprint for designing robust and resilient neural networks. The simulation of biological brain behavior in controlled environments also affords the opportunity to investigate more deeply on how animal brains function, thus providing inspiration for future artificial intelligence research.

ACKNOWLEDGMENT

The authors acknowledge the use of Google Gemini to improve the language, grammar, and clarity of this paper.

REFERENCES

- [1] F. Rosenblatt, "The perceptron: a probabilistic model for information storage and organization in the brain." *Psychological review*, vol. 65, no. 6, p. 386, 1958.
- [2] Y. LeCun, B. Boser, J. Denker, D. Henderson, R. Howard, W. Hubbard, and L. Jackel, "Handwritten digit recognition with a back-propagation network," in *Advances in Neural Information Processing Systems*, D. Touretzky, Ed., vol. 2. Morgan-Kaufmann, 1989.
- [3] A. Krizhevsky, I. Sutskever, and G. E. Hinton, "Imagenet classification with deep convolutional neural networks," in *Advances in Neural Information Processing Systems*, F. Pereira, C. Burges, L. Bottou, and K. Weinberger, Eds., vol. 25. Curran Associates, Inc., 2012.
- [4] P. J. Werbos, "Backpropagation through time: what it does and how to do it," *Proceedings of the IEEE*, vol. 78, no. 10, pp. 1550–1560, 2002.
- [5] S. Hochreiter and J. Schmidhuber, "Long short-term memory," *Neural computation*, vol. 9, no. 8, pp. 1735–1780, 1997.
- [6] A. Vaswani, N. Shazeer, N. Parmar, J. Uszkoreit, L. Jones, A. N. Gomez, Ł. Kaiser, and I. Polosukhin, "Attention is all you need," *Advances in neural information processing systems*, vol. 30, 2017.
- [7] Y. Shueb, A. Nowzad, and H. Gottschalk, "Out-of-distribution segmentation in autonomous driving: Problems and state of the art," in *Proceedings of the Computer Vision and Pattern Recognition Conference*, 2025, pp. 4310–4320.
- [8] A. Ceccarelli and F. Secci, "Rgb cameras failures and their effects in autonomous driving applications," *IEEE Transactions on Dependable and Secure Computing*, vol. 20, no. 4, pp. 2731–2745, 2022.
- [9] Y. Zhu, "The drosophila visual system: From neural circuits to behavior," *Cell adhesion & migration*, vol. 7, no. 4, pp. 333–344, 2013.
- [10] A. Borst and L. N. Groschner, "How flies see motion," *Annual review of neuroscience*, vol. 46, no. 1, pp. 17–37, 2023.
- [11] D. B. Turner-Evans, K. T. Jensen, S. Ali, T. Paterson, A. Sheridan, R. P. Ray, T. Wolff, J. S. Lauritzen, G. M. Rubin, D. D. Bock, *et al.*, "The neuroanatomical ultrastructure and function of a biological ring attractor," *Neuron*, vol. 108, no. 1, pp. 145–163, 2020.
- [12] Y. E. Fisher, "Flexible navigational computations in the drosophila central complex," *Current opinion in neurobiology*, vol. 73, p. 102514, 2022.
- [13] P. Qin, T. Zhao, Q. Su, and H. Yang, "Mobile robot navigation via domain randomization and real-world adaptation," in *2025 IEEE International Conference on Unmanned Systems (ICUS)*. IEEE, 2025, pp. 878–883.
- [14] M. Zhang, S. Duan, and C. Xu, "Robot vision-based autonomous navigation method using sim2real domain adaptation," in *2024 IEEE International Symposium on Parallel and Distributed Processing with Applications (ISPA)*. IEEE, 2024, pp. 1203–1209.
- [15] Y. Suresh, V. Devashya, *et al.*, "Liquid neural networks for autonomous driving: A framework for intelligent decision-making," in *2025 5th International Conference on Emerging Research in Electronics, Computer Science and Technology (ICERECT)*. IEEE, 2025, pp. 1–6.
- [16] M. Chahine, R. Hasani, P. Kao, A. Ray, R. Shubert, M. Lechner, A. Amini, and D. Rus, "Robust flight navigation out of distribution with liquid neural networks," *Science Robotics*, vol. 8, no. 77, p. eadc8892, 2023.
- [17] E. Aasi, P. Nguyen, S. Sreeram, G. Rosman, S. Karaman, and D. Rus, "Generating out-of-distribution scenarios using language models," in *2025 IEEE International Conference on Robotics and Automation (ICRA)*. IEEE, 2025, pp. 10 616–10 623.
- [18] Y. Qiao, W. Lyu, H. Wang, Z. Wang, Z. Li, Y. Zhang, M. Tan, and Q. Wu, "Open-nav: Exploring zero-shot vision-and-language navigation in continuous environment with open-source llms," in *2025 IEEE International Conference on Robotics and Automation (ICRA)*. IEEE, 2025, pp. 6710–6717.
- [19] M. Przewiezlikowski, M. Smieja, L. Struski, and J. Tabor, "Misconv: Convolutional neural networks for missing data," in *Proceedings of the IEEE/CVF Winter Conference on Applications of Computer Vision (WACV)*, January 2022, pp. 2060–2069.
- [20] K. Kassaw, F. Luzi, L. M. Collins, and J. M. Malof, "Are deep learning models robust to partial object occlusion in visual recognition tasks," *Pattern Recognition*, vol. 171, p. 112215, 2026.
- [21] N. Patel, A. Choromanska, P. Krishnamurthy, and F. Khorrami, "A deep learning gated architecture for ugv navigation robust to sensor failures," *Robotics and Autonomous Systems*, vol. 116, pp. 80–97, 2019.
- [22] S. Dorkenwald, A. Matsliah, A. R. Sterling, P. Schlegel, S.-C. Yu, C. E. McKellar, A. Lin, M. Costa, K. Eichler, Y. Yin, *et al.*, "Neuronal wiring diagram of an adult brain," *Nature*, vol. 634, no. 8032, pp. 124–138, 2024.
- [23] P. Schlegel, Y. Yin, A. S. Bates, S. Dorkenwald, K. Eichler, P. Brooks, D. S. Han, M. Gkantia, M. Dos Santos, E. J. Munnelly, *et al.*, "Whole-brain annotation and multi-connectome cell typing of drosophila," *Nature*, vol. 634, no. 8032, pp. 139–152, 2024.
- [24] J. K. Lappalainen, F. D. Tschopp, S. Prakhya, M. McGill, A. Nern, K. Shinomiya, S.-y. Takemura, E. Gruntman, J. H. Macke, and S. C. Turaga, "Connectome-constrained networks predict neural activity across the fly visual system," *Nature*, vol. 634, no. 8036, pp. 1132–1140, 2024.
- [25] P. K. Shiu, G. R. Sterne, N. Spiller, R. Franconville, A. Sandoval, J. Zhou, N. Simha, C. H. Kang, S. Yu, J. S. Kim, *et al.*, "A drosophila computational brain model reveals sensorimotor processing," *Nature*, vol. 634, no. 8032, pp. 210–219, 2024. [Online]. Available: <https://www.nature.com/articles/s41586-024-07763-9>
- [26] S. R. Walker, M. Peña-Garcia, and A. V. Devineni, "Connectomic analysis of taste circuits in drosophila," *Scientific Reports*, vol. 15, no. 1, p. 5278, 2025.
- [27] E. Todorov, T. Erez, and Y. Tassa, "Mujoco: A physics engine for model-based control," in *2012 IEEE/RSJ International Conference on Intelligent Robots and Systems*, 2012, pp. 5026–5033.
- [28] M. Tan and Q. Le, "EfficientNet: Rethinking model scaling for convolutional neural networks," in *Proceedings of the 36th International Conference on Machine Learning*, ser. Proceedings of Machine Learning Research, K. Chaudhuri and R. Salakhutdinov, Eds., vol. 97. PMLR, 09–15 Jun 2019, pp. 6105–6114.
- [29] A. Howard, M. Sandler, G. Chu, L.-C. Chen, B. Chen, M. Tan, W. Wang, Y. Zhu, R. Pang, V. Vasudevan, Q. V. Le, and H. Adam, "Searching for mobilenetv3," in *Proceedings of the IEEE/CVF International Conference on Computer Vision (ICCV)*, October 2019.
- [30] D. J. Watts and S. H. Strogatz, "Collective dynamics of 'small-world' networks," *nature*, vol. 393, no. 6684, pp. 440–442, 1998.

- [31] H. Kalmus, "Anemotaxis in drosophila," *Nature*, vol. 150, no. 3805, pp. 405–405, 1942.
- [32] G. Boekhoff-Falk and D. F. Eberl, "The drosophila auditory system," *Wiley Interdisciplinary Reviews: Developmental Biology*, vol. 3, no. 2, pp. 179–191, 2014.
- [33] S. Ross, G. Gordon, and D. Bagnell, "A reduction of imitation learning and structured prediction to no-regret online learning," in *Proceedings of the fourteenth international conference on artificial intelligence and statistics*. JMLR Workshop and Conference Proceedings, 2011, pp. 627–635.
- [34] I. Ulrich and J. Borenstein, "Vfh*: local obstacle avoidance with look-ahead verification," in *Proceedings 2000 ICRA. Millennium Conference. IEEE International Conference on Robotics and Automation. Symposia Proceedings (Cat. No.00CH37065)*, vol. 3, 2000, pp. 2505–2511 vol.3.
- [35] D. S. Bassett and E. T. Bullmore, "Small-world brain networks revisited," *The Neuroscientist*, vol. 23, no. 5, pp. 499–516, 2017.
- [36] S. Xie, A. Kirillov, R. Girshick, and K. He, "Exploring randomly wired neural networks for image recognition," in *Proceedings of the IEEE/CVF international conference on computer vision*, 2019, pp. 1284–1293.